

Supplemental Document for Automatically Determining the Confocal Parameters from OCT B-Scans for Quantification of the Attenuation Coefficients

Nicholas Dwork[†], Gennifer T. Smith[†], Theodore Leng,
John M. Pauly, and Audrey K. Bowden

APPENDIX A SIGNAL MODEL

Since OCT systems typically collect data one A-scan at a time (a single longitudinal scan), we consider the intensity at each depth z of an A-scan, which may be modeled as

$$I_f(z) = h(z) f(z) \beta r(z) \exp\left(-2 \int_0^z \mu(\epsilon) d\epsilon\right), \quad (1)$$

where f models the fall-off effect [1], [2], I_f denotes inclusion of the fall-off function in the signal model, β is a constant of proportionality (which accounts for such factors as the quantum efficiency of the detector, the coherence length, the size of the detector, and the intensity of the light source), $r(z)$ is the fraction of scattered light that is backscattered from depth z , $\mu(z)$ is the attenuation coefficient at depth z , and ϵ is a variable of integration [3].

The function h is called the confocal function; it describes the intensity profile emitted from and coupled back into the fiber as a function of depth [4], [5], [6]. It is parameterized by two quantities: the focal plane depth (z_0) and the apparent Rayleigh range (z_R) defined as

$$z_R = \alpha n z_r, \quad (2)$$

where $\alpha = 2$ for diffuse reflectors, n is the index of refraction, and z_r is the Rayleigh range of the scanning lens [5]. The model of the confocal function for intensity is

$$h(z) = \left(\left(\frac{z - z_0}{z_R} \right)^2 + 1 \right)^{-1}. \quad (3)$$

Equation (1) models the intensity at each depth. The m^{th} sample obtained from a (one-sided) M -point A-scan (after resampling, apodization, and DC subtraction performed on the detected spectrum) corresponds to an integration of the signal I_f :

$$\mathbf{I}_f[m] = \int_{z_m}^{z_{m+1}} I_f(z) dz, \quad (4)$$

where z_m and z_{m+1} are the bounds of the m^{th} pixel, and $\mathbf{I}_f \in \mathbb{R}^M$. The model may be further extended to incorporate

additive noise sources such as read-out noise, digitizer noise, and dark current:

$$\mathbf{I}_f^{(c)}[m] = \mathbf{I}_f[m] + \mathbf{c}[m], \quad (5)$$

where $\mathbf{c} \in \mathbb{R}^M$ is a vector of independent identically distributed (i.i.d.) random variables with mean \bar{c} . The superscript (c) denotes that this signal model accounts for additive noise.

Note that (5) does not account for speckle, which is a multiplicative noise source [7]. The inputs to autoConfocal are B-scans with the speckle removed; we discuss this in detail in §III-C in the main manuscript. Equation (5) is the most complete model for a discrete A-scan that is used throughout the main manuscript.

APPENDIX B ESTIMATING THE ATTENUATION COEFFICIENTS

Once the focal plane and the apparent Rayleigh range are estimated by solving (6) of the main manuscript, the attenuation coefficient for each pixel can be determined using DRC [8]. To remove the effects of the confocal function without amplifying any remaining noise, the measured data from the first B-scan (the discrete signal $\mathbf{I}_{f,1}$) is filtered with a restoration filter $\tilde{\mathbf{I}}[m] = \mathbf{I}_{f,1}[m] \mathbf{H}_{\text{res}}[m]$ [9], where

$$\mathbf{H}_{\text{res}}[m] = \frac{1}{\mathbf{f}[m] \mathbf{h}[m]} \frac{|\mathbf{I}_{f,1}[m]|^2}{|\mathbf{I}_{f,1}[m]|^2 + \gamma}. \quad (6)$$

In the filter, \mathbf{f} and \mathbf{h} are vectors representing the value of the fall-off function and the confocal function at each pixel, respectively. The variable γ is a regularization parameter of the algorithm related to the noise power present in the imagery (specified by the user); it is constant for a given system and type of sample. The restoration filter optimally eliminates the effects of the confocal function, which permits estimation of the attenuation coefficients even when the confocal function is in the sample.

Once $\tilde{\mathbf{I}}$ has been determined, the vector of attenuation coefficients $\hat{\boldsymbol{\mu}}$ is estimated as follows:

$$\hat{\boldsymbol{\mu}}[m] \approx \frac{\tilde{\mathbf{I}}[m]}{2 s_z \sum_{r=m}^M \tilde{\mathbf{I}}[r]}, \quad (7)$$

where s_z is the axial size of an individual pixel.

[†] These authors contributed equally to this work.

Since the confocal function is a parameter of the imaging system (in a given configuration), DRC can be applied to all subsequent images as long as z_0 and z_R are unchanged¹. Therefore, while determination of the confocal function parameters requires two B-scans with in-plane rotation and translation, this is not a limitation on the other B-scans acquired during the session.

APPENDIX C NUMERICAL SIMULATIONS

In this appendix, we review the design of and insights gained from numerical simulations.

A. Experimental Design

We performed numerical simulations to understand the requirements of the autoConfocal algorithm. The results show how precise autoConfocal must be in order to yield accurate estimates with DRC.

We simulated shot-noise-limited B-scans as was done in [8]. Zero-mean Gaussian noise was added to each A-scan independently with a variance chosen to match an SNR of 40 dB (typical of OCT imaging systems). The simulated phantom was 2 mm in depth: the upper half had an attenuation coefficient of 1 mm^{-1} and the lower half had an attenuation coefficient of 4 mm^{-1} , as shown in Fig. 1 (a). These values were chosen to mimic those found in biological tissues (e.g., bladder tissue). A focal plane location of 0.5 mm and three Rayleigh ranges (0.050 mm, 0.106 mm, and 0.2238 mm) were used in the simulation. The true value of the focal plane position was kept constant at a depth of 0.5 mm while the focal plane input to DRC varied from 0.35 to 0.65 mm. We tested an error in the Rayleigh range from -0.1 mm to 0.15 mm .

B. Results

To quantify the error in the attenuation coefficient estimates during simulation, we used the excess energy metric e defined as follows:

$$e[m] = \frac{\|\boldsymbol{\mu}(1:m) - \boldsymbol{\mu}_{\text{true}}(1:m)\|_2}{\|\boldsymbol{\mu}_{\text{true}}\|_2}. \quad (8)$$

The excess error energy metric is a relative metric that quantifies changes in accuracy of the estimate vector $\boldsymbol{\mu}$ for a given vector of known attenuation coefficients $\boldsymbol{\mu}_{\text{true}}$. Details about the set-up of the simulations and the excess error energy metric can be found in [8].

The energy error depth d_e , defined in [8] to be the depth at which the excess energy e exceeded 5%, was measured for each column of a 100×201 element simulation, and the reported value is the average over all the columns (A-scans). Larger values of d_e (located near the bottom of the

y-axis) correspond to better estimates of the actual attenuation coefficients and are more desired.

Fig. 1 shows the effect of different system properties on the energy error depth. Figure 1 (b) shows how d_e is reduced as the error in the focal plane estimate increases. The horizontal axis indicates the deviation (offset) between the actual and specified focal planes. This simulation indicates that any error in the estimated focal plane less than 100% of the Rayleigh range will reduce the energy error depth by less than 10% (the bars in the figure show $\pm 100\%$ of the Rayleigh range), which we define as the tolerable error. Therefore, for accurate estimates of the attenuation coefficient, the focal plane location determined using autoConfocal must be within 100% of the true value of the Rayleigh range. Fig. 1 (c) shows how d_e is reduced as the magnitude of the error in the Rayleigh range estimate increases. Here, the horizontal axis indicates the deviation (offset) in the actual and specified Rayleigh ranges. This simulation indicates that any error in the estimated Rayleigh range less than 125% of the Rayleigh range will reduce the energy error depth by less than 10% (the bars in the figure represent $\pm 125\%$ of the Rayleigh range). Therefore, for accurate attenuation coefficient estimates, the Rayleigh range determined using autoConfocal must be within 125% of the true value of the Rayleigh range.

APPENDIX D ATTENUATION OF THE PHANTOM

For each layer of the phantom, approximate attenuation coefficients at 850 nm (μ_{850}) were calculated using [10]:

$$\mu_{850} = 21.56\nu - 0.11,$$

where ν is the weight percentage of TiO_2 . The attenuation coefficients were scaled to a center wavelength of 1325 nm using a power law [11]:

$$\mu_{\lambda_2} = (\lambda_1/\lambda_2)^{\text{SP}}(\mu_{\lambda_1}),$$

where SP is the scattering power and is related to the average size of the scatterers. A scattering power of 1.9 was used for TiO_2 [12]. Layer 1 of the phantom was made with a high concentration of TiO_2 (weight percentage of 0.29, approximate attenuation coefficient of 2.6 mm^{-1}). Layers 2 and 4 were made with a low concentration of TiO_2 (weight percentage of 0.05, approximate attenuation coefficient of 0.42 mm^{-1}). Layer 3 was made with a medium concentration (weight percentage of 0.20, approximate attenuation coefficient of 1.8 mm^{-1}). Layer 5 was made with a very high concentration of TiO_2 (weight percentage of 0.87, approximate attenuation coefficient of 8.0 mm^{-1}).

We used an index of refraction of 1.4 for the PDMS/ TiO_2 mixtures when calculating the true apparent Rayleigh range for the phantom [13]. The index of refraction was assumed constant for all layers, which reflects the assumption that the concentration of TiO_2 is too small to significantly affect the refractive index of the PDMS [14], as suggested by the Lorentz-Lorenz mixing rule.

¹Since the eye is part of the imaging system in ophthalmic imaging, one may suspect that the imaging system will change (and therefore a recalibration will have to be done for every new B-scan). However, during an OCT imaging session, the patient is asked to maintain a far-field of focus and direct his view at a specific fixed location. As long as the patient is able to maintain this state, the imaging system should remain approximately constant.

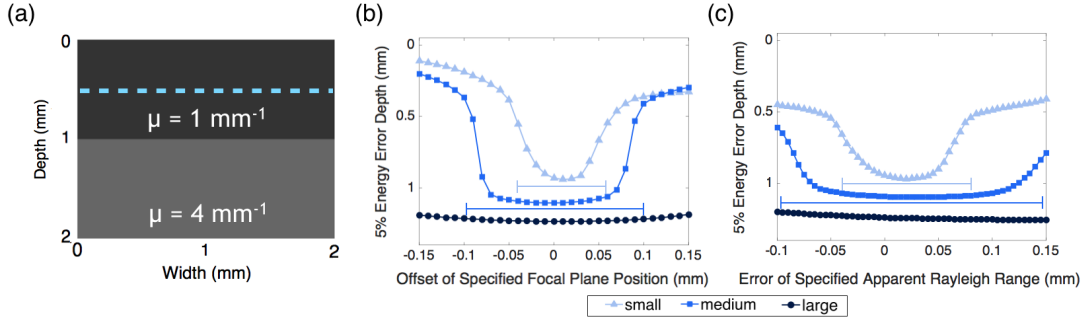


Fig. 1: The energy error depth d_e is calculated for the phantom shown in (a); errors are simulated for three different Rayleigh ranges: small (0.050 mm), medium (0.106 mm), and large (0.238 mm). The simulation phantom is shown in (a) (the blue dashed line indicates the focal plane position), (b) shows how d_e changes with errors in the estimated focal plane, and (c) shows how d_e changes with errors in the estimated Rayleigh range. For the focal plane and Rayleigh range, errors of approximately 100% and 125% of the Rayleigh range (indicated by the horizontal bars), respectively, can be tolerated and still attain accurate results. Horizontal bars for the large Rayleigh range simulated are not shown as they extend far beyond the bounds of the image.

A. Phantom Experiment: Additional Results

Table I shows the results of autoConfocal (estimates of the focal plane and apparent Rayleigh range) on the phantom when the two B-scans are related by different lateral translations and rotations. Recall that the true values of the focal plane and apparent Rayleigh range are 1.6 mm and 0.30 mm, respectively. As the translation and/or rotation values are increased, there is less overlap between the two B-scans, which generally results in higher error of the autoConfocal algorithm. Additionally, the approximation of the rotation as a shear is less accurate for large rotations (e.g., 20°), which results in higher error. This table shows that if the magnitude of lateral translation is 0.5 mm or less and the magnitude of rotation is 10 degrees or less then the estimates produced by autoConfocal are accurate. These amounts correspond to an overlap of greater than 2 mm^2 for the phantom data. These limits are within the error of the eye-tracking of clinical systems, as seen in §V-C. The asymmetric trend in the error with respect to translation reflects the asymmetric structure of the phantom.

To assess the uncertainty of the estimated attenuation coefficients in the phantom, we calculated attenuation coefficients for all datasets shown in Table I that have a rotation of less than 10° and a translation of magnitude less than 0.5 mm (15 datasets in total). Fig. 2 shows the standard deviation of the attenuation coefficient estimates. The vast majority of estimates have a standard deviation of less than 0.2 mm^{-1} .

To assess the uncertainty in the estimates of the confocal function parameters, we collected pairs of B-scans from 8 different locations within the sample with varying structure. The focal plane was fixed at 1.5 mm and the apparent Rayleigh range (determined by modifying the manufacturer's supplied Rayleigh range using (3) from the manuscript) was 0.30 mm. The mean and standard deviation of the autoConfocal estimates for the focal plane and apparent Rayleigh range was $1.5 \pm 0.1 \text{ mm}$ and $0.37 \pm 0.06 \text{ mm}$, respectively. These values are within the tolerance for accurate estimation of the

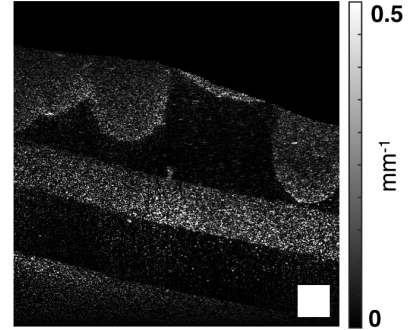


Fig. 2: Standard Deviation of the attenuation coefficient estimates of the reference image of the phantom used in the sensitivity analysis. The vast majority of estimates have a standard deviation less than 0.2 mm^{-1} . The white square represents $0.25 \times 0.25 \text{ mm}^2$.

attenuation coefficients.

APPENDIX E AUTOCONFOCAL AND FALL-OFF

Fall-off is an effect related to the resolution of the spectrometer in an SD-OCT system. Yun et al. present a model for fall-off which is an explicit function of spectrometer and CCD parameters as follows [1]:

$$f(z) = \left(\frac{\sin \zeta}{\zeta} \right)^2 \exp \left(- \frac{\left(\frac{d\lambda}{\Delta\lambda} \right)^2}{2 \ln 2} \zeta^2 \right), \quad (9)$$

where $\delta\lambda$ is the spectrometer's Full-Width Half Max (FWHM) resolution, $\Delta\lambda$ is the wavelength spacing between pixels, and $\zeta = (\pi/2) (4z\Delta\lambda/\lambda_0^2)$ with central source wavelength λ_0 . Since the fall-off is largely a property of the geometry of the imaging system, for many systems it would only need to be determined once (since that part of the geometry is fixed).

If the fall-off is not known or cannot be determined then the fall-off effect can be neglected, as can be seen in (6) of

z_0/z_R (mm)/(mm)		Lateral Translations (mm)						
		-0.75	-0.5	-0.25	0	0.25	0.5	0.75
Rotations (°)	0	1.54 / 0.53	1.57 / 0.54	1.58 / 0.54	1.62 / 0.55	1.64 / 0.60	1.66 / 0.63	1.69 / <u>0.69</u>
	5	1.62 / 0.54	1.58 / 0.58	1.59 / 0.59	1.61 / 0.56	1.62 / 0.51	1.62 / 0.50	1.62 / 0.50
	10	1.65 / 0.59	1.65 / 0.54	1.64 / 0.53	1.65 / 0.49	1.61 / 0.47	1.60 / 0.47	1.58 / 0.45
	15	<u>1.71</u> / 0.57	<u>1.73</u> / 0.53	1.67 / 0.55	1.67 / 0.47	1.63 / 0.44	1.60 / 0.41	1.58 / 0.41
	20	<u>1.85</u> / <u>0.67</u>	<u>1.76</u> / 0.62	1.69 / 0.60	1.69 / 0.61	1.69 / <u>0.79</u>	1.60 / 0.62	<u>-0.52</u> / 0.01

TABLE I: AutoConfocal estimates on phantom data when the B-scans are related by various lateral translations and rotations. True values for the focal plane location (z_0) and apparent Rayleigh range (z_R) are 1.6 mm and 0.30 mm, respectively. Values outside of the tolerable error (100% and 125% of the Rayleigh range for the focal plane position and Rayleigh range, respectively) for accurately estimating the attenuation coefficient are underlined.

the main manuscript, whenever the difference in intensity due to the confocal function (in decibels) is large compared to the difference due to fall-off effects. That is, whenever

$$\begin{aligned} \hat{\mathbf{I}}_{f,1}^{(dB)}(n, m) - \hat{\mathbf{I}}_{f,2}^{(dB)}(n', m') \\ \approx \hat{\mathbf{I}}_1^{(dB)}(n, m) - \hat{\mathbf{I}}_2^{(dB)}(n', m'). \end{aligned}$$

If this is the case, then the confocal parameters can be determined by solving the following optimization problem:

$$\begin{aligned} \underset{z_0, z_R}{\text{minimize}} \quad & \left\| \left[\hat{\mathbf{I}}_{f,1}^{(dB)}(n, m) - \hat{\mathbf{I}}_{f,2}^{(dB)}(n', m') \right] - \right. \\ & \left[10 \log_{10} \left(\left(\frac{z + \Delta z + Z_n - z_0}{z_R} \right)^2 + 1 \right) - \right. \\ & \left. \left. 10 \log_{10} \left(\left(\frac{z - z_0}{z_R} \right)^2 + 1 \right) \right] \right\|_{w,1} \\ \text{subject to } & z_R > 0. \end{aligned} \quad (10)$$

These conditions will be met when the surface of one of the B-Scans in the optimization problem is near the focal plane (approximately within half of the Rayleigh range).

The fall-off parameters for the TELESTO system used in §V of the main manuscript were determined by fitting the model of (9) to data of a neutral density filter imaged at several depths, which yielded $\delta\lambda = 0.11$ nm and $\Delta\lambda = 0.07$ nm/pixel. This results in a maximum reduction due to fall-off of 50% at an imaging depth of 2.57 mm (corresponding to a fall-off rate of approximately 2.3 dB per mm). This is a significant reduction. However, with the TELESTO system, the difference in intensity due to the confocal function with one sample located near the focal plane and the other located a Rayleigh range away could be greater than 50%. That is, the same reduction due to fall-off over the entire imaging range (2.57 mm for the TELESTO data shown) can be observed over a much shorter distance (0.1 mm for the TELESTO data shown) due to the confocal function. Therefore, the additional reduction due to fall-off in this case could be neglected.

To verify this, we reproduced the analysis of Table I with fall-off taken into account. The differences in the confocal function's parameters determined with autoConfocal with and without fall-off taken into account are shown in Table II. The differences are insignificant for rotations of less than 15° and translations with magnitude less than 0.75 mm. (Note that the focal plane location moves slightly more than 0.1 mm

after taking fall-off into account with a rotation of 0 degrees and a translation of 0.5 mm. We imaged the sample through ultrasound gel, and the gel does not have a uniform thickness above the sample. We suspect that this non-uniformity has led to an anomalously large error.)

We also did further analysis on the *ex-vivo* rabbit tissue. For the results shown in §V-B of the main manuscript, the focal plane and apparent Rayleigh range determined with fall-off taken into account are 0.77 mm and 0.22 mm, respectively. This is a negligible difference from the focal plane and Rayleigh range determined without accounting for fall-off, which are 0.77 mm and 0.20 mm, respectively. The attenuation coefficients calculated from the B-scans of this data are shown in Fig. 3; (a) and (b) show the attenuation coefficient maps calculated with fall-off taken into account, and (c) and (d) show the corresponding attenuation coefficient maps without taking fall-off into account. Note that there is no appreciable difference between the two sets of maps.

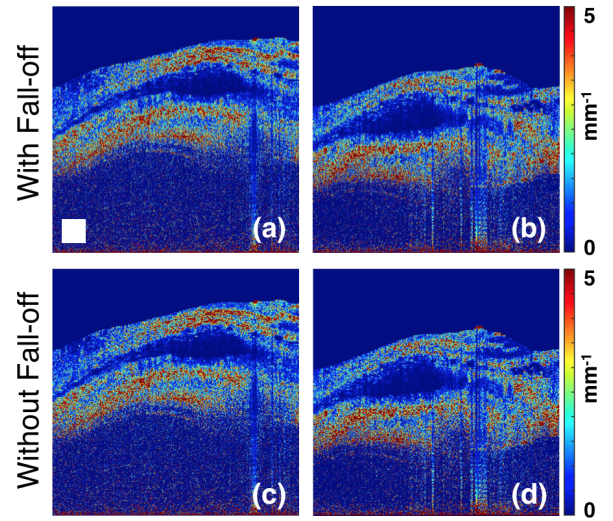


Fig. 3: Attenuation coefficient maps calculated from the B-scans of *ex-vivo* rabbit eye using data collected with a TELESTO SD-OCT system. Figures (a) and (b) show the attenuation coefficient maps with fall-off taken into account; figures (c) and (d) show the corresponding attenuation coefficient maps without taking fall-off into account. There is not a significant difference between the two sets of maps. The white square in (a) represents 0.25×0.25 mm².

z_0/z_R (mm)/(mm)		Lateral Translations (mm)						
		-0.75	-0.5	-0.25	0	0.25	0.5	0.75
Rotations (°)	0	0.05 / 0.04	0.07 / 0.03	0.08 / 0.02	0.08 / 0.02	0.09 / 0.02	<u>0.11</u> / 0.01	<u>0.13</u> / 0.01
	5	0.07 / 0.03	0.06 / 0.03	0.08 / 0.02	0.08 / 0.01	0.07 / 0.01	0.07 / 0.00	0.07 / 0.00
	10	0.06 / 0.02	0.06 / 0.01	0.07 / 0.03	0.06 / 0.00	0.06 / 0.00	0.06 / 0.00	0.07 / 0.00
	15	0.02 / -0.01	0.06 / 0.00	0.06 / 0.01	0.06 / -0.01	0.04 / 0.04	0.05 / 0.01	0.07 / 0.00
	20	0.06 / 0.02	0.06 / 0.00	0.07 / 0.01	0.04 / 0.02	<u>0.64</u> / -0.01	0.08 / -0.01	<u>0.15</u> / -0.06

TABLE II: Difference between confocal parameters calculated with and without accounting for the fall-off effect. The underlined values show where the differences are above the tolerances of 0.1 mm for the focal plane and 0.37 mm for the apparent Rayleigh range.

For the same data, we removed the effect of the fall-off present in the TELESTO system as described in §III-A of the main manuscript and then imposed synthetic fall-offs of different amounts (modeled as Gaussian functions with different standard deviations). For each amount of fall-off, we used autoConfocal to estimate the confocal function's parameters; the results are shown in Fig. 4. For both the apparent Rayleigh range and focal plane estimation, a fall-off of less than 7 dB per mm (the maximum amount of fall-off simulated) yields estimates that are within the tolerance (125% and 100% of a Rayleigh range for the Rayleigh range and focal plane, respectively) for generating accurate estimates of the attenuation coefficients. The amount of fall-off in the Cirrus system is less than this cut-off (the system has fall-off less than 5.5 dB per mm depth in tissue) and therefore, we are able to neglect fall-off without compromising the autoConfocal results.

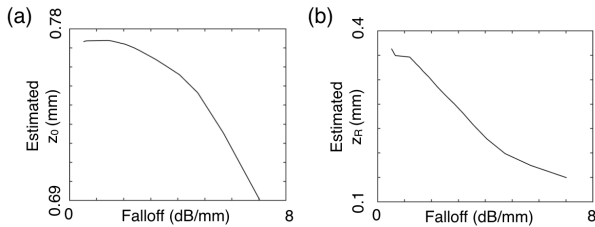


Fig. 4: Estimates of the confocal function parameters generated by autoConfocal with different amounts of fall-off imposed on the data. (a) Estimated focal plane with varying amounts of fall-off. (b) Estimated apparent Rayleigh range for varying amounts of fall-off. For all fall-off rates tested, all estimates were within tolerable range for accurate quantification of the attenuation coefficients.

REFERENCES

- [1] S. Yun, G. Tearney, B. Bouma, B. Park, and J. de Boer, "High-Speed Spectral-Domain Optical Coherence Tomography at 1.3 μm Wavelength," *Optics Express*, vol. 11, no. 26, pp. 3598–3604, 2003.
- [2] M. Hagen-Eggert, P. Koch, and G. Hüttmann, "Analysis of the signal fall-off in spectral domain optical coherence tomography systems," in *Proc. SPIE*, vol. 8213, 2012, pp. 82131K–82131K.
- [3] K. A. Vermeer, J. Mo, J. J. A. Weda, H. G. Lemij, and J. F. de Boer, "Depth-resolved model-based reconstruction of attenuation coefficients in optical coherence tomography," *Biomedical Optics Express*, vol. 5, no. 1, pp. 322–337, 2013.

- [4] T. G. van Leeuwen, D. J. Faber, and M. C. Aalders, "Measurement of the axial point spread function in scattering media using single-mode fiber-based optical coherence tomography," *IEEE Journal of Selected Topics in Quantum Electronics*, vol. 9, no. 2, pp. 227–233, 2003.
- [5] D. J. Faber, F. J. van der Meer, M. C. G. Aalders, and T. G. van Leeuwen, "Quantitative measurement of attenuation coefficients of weakly scattering media using optical coherence tomography," *Optics Express*, vol. 12, no. 19, pp. 4353–4365, 2004.
- [6] M. Hohmann, B. Legenfelder, R. Kanawade, F. Klämpfl, and M. Schmidt, "Extension of depth-resolved reconstruction of attenuation coefficients in optical coherence tomography for slim samples," in *Biophotonics Japan 2015*, vol. 9792, Dec. 2015, p. 97920P.
- [7] J. M. Schmitt, S. Xiang, and K. M. Yung, "Speckle in optical coherence tomography," *Journal of biomedical optics*, vol. 4, no. 1, pp. 95–106, 1999.
- [8] G. T. Smith, N. Dwork, D. O'Connor, U. Sikora, K. L. Lurie, J. M. Pauly, and A. K. Ellerbee, "Automated, depth-resolved estimation of the attenuation coefficient from optical coherence tomography data," *Medical Imaging, IEEE Transactions on*, vol. 34, no. 12, pp. 2592–2602, 2015.
- [9] R. N. Bracewell, *Two-Dimensional Imaging*. Prentice-Hall, Inc., 1995, pp. 477–478.
- [10] D. M. M. de Bruin, R. H. Bremmer, V. M. Kodach, R. de Kinkelder, J. van Marle, T. G. van Leeuwen, and D. J. Faber, "Optical phantoms of varying geometry based on thin building blocks with controlled optical properties," *Journal of biomedical optics*, vol. 15, no. 2, p. 025001, 2010.
- [11] V. Kodach, J. Kalkman, D. Faber, and T. G. van Leeuwen, "Quantitative comparison of the OCT imaging depth at 1300 nm and 1600 nm," *Biomedical optics express*, vol. 1, no. 1, pp. 176–185, 2010.
- [12] X. Zha, "Image processing of optical coherence tomography for image guided dental drilling," *Masters thesis, Delft University of Technology*, 2011.
- [13] M. Querry, "Optical constants of minerals and other materials from the millimeter to the ultraviolet," Chemical Research Development and Engineering Center Aberdeen Proving Ground, Tech. Rep., 1987.
- [14] S. Motakef, T. Suratwala, R. Roncome, J. Boulton, G. Teowee, and D. Uhlmann, "Processing and optical properties of inorganic-organic hybrids (polycerams). ii. pdms-based waveguides," *Journal of non-crystalline solids*, vol. 178, pp. 37–43, 1994.